Title

Synthesis and Design of Programmable Subwavelength Coil Array for Near-Field Manipulation

Permalink

https://escholarship.org/uc/item/85q8q4xj

Authors

Gao, F
Zhang, F
Wakatsuchi, H
et al.

Publication Date

2015-07-15

DOI

10.1109/TMTT.2015.2450711

Peer reviewed

Synthesis and Design of Programmable Subwavelength Coil Array for Near-Field Manipulation

Fei Gao, *Student Member, IEEE*, Fushun Zhang, Hiroki Wakatsuchi, *Member, IEEE*, and Daniel F. Sievenpiper, *Fellow, IEEE*

Abstract—We present the design and experimental demonstration of a programmable subwavelength coil array, which can manipulate the evanescent magnetic field leading to a precisely controlled electric-field pattern at an image plane in the near-field zone. A synthesis methodology is outlined for 2-D near-field manipulations. Simulation based on a full-wave electromagnetic solver clearly demonstrates the focused electric-field pattern, and its implementation is discussed. An example of a three-layer subwavelength coil array with 48 units is fabricated and measured. The consensus of the measured results with the simulated and synthesized results verified the presented synthesis method. Such a device, capable of producing a programmable magnetic field and electric field, respectively, in orthogonal planes, will find applications in biomedical devices such as neural stimulation, and potentially other areas such as noncontact charging.

Index Terms—Electrically small, near-field, subwavelength array, synthesis, transcranial magnetic stimulation (TMS).

I. INTRODUCTION

ELECTROMAGNETIC near-field research has received considerable attention since Synge showed that detecting the near-field of an object equates to tapping into the object's subwavelength details, which can obtain resolution beyond the diffraction limit [1]. Experimental verification showing that near-field imaging is possible has been reported [2], [3]. In addition to optical imaging, near-field manipulation and focusing of the electromagnetic field as a key technique in both optical

and microwave regimes has intrigued scientists and engineers alike. Techniques for subwavelength focusing in near-field include superlenses [4], aperiodic gold nanowire arrays [5], subwavelength spaced slot arrays [6], dielectric gratings [7], and a near-field plate based on radiationless interference [8]–[11]. In addition to focusing the electric field, manipulation of the magnetic field in the near-field zone is also intriguing and its implementation has been reported [12]–[14]. In principle, the methodology pertaining to near-field focusing can lead to all desired near-field patterns based on the complicated design of a near-field plate. In previous work, a programmable magnetic screen controlled by switches surrounding the plate was designed, which can focus a magnetic field into 256 different spots [14]. However, it is still difficult to obtain an arbitrary near-field pattern using the passive near-field plate due to the limited freedom in adjusting the configuration of the near-field plate.

Apart from the near-field plate, the development of near-field targeted antenna arrays is motivated by the increasing interest in the applications of near-field communication [15]–[18], non-contact microwave detection systems [19], and vital life detection systems [20]. Similar to conventional antenna arrays, the use of more than one source leads to the higher freedom in design, and more flexible and complex near-field patterns are obtained compared to the near-field plates [21], [22]. Different from the far-field zone of the array, the electric field and magnetic field have a more complicated relationship, and the applications based on the electric field or magnetic field in the near-field zone vary significantly. While near-field arrays are often applied to the electric field, only few such active arrays have been suggested for magnetic-field focusing. A 2-D subwavelength array of resonant capacitively loaded loops for magnetic-field focusing was presented recently [23]. It seems otherwise that only symmetrical near-field patterns have been discussed. Asymmetrical magnetic-field patterns, and the electric field focusing in terms of position and polarization in the near-field zone, to our knowledge, has not been demonstrated.

In the field of neuroscience, an important goal is to modulate neural activity [24]. The electroencephalogram (EEG) and functional magnetic resonance imaging (fMRI) provide good ways to read signals from the brain and efforts are underway to improve their resolution [25]–[27]. However, noninvasive methods to precisely write neural signals into the brain are still lacking. Biomedical applications such as transcranial magnetic
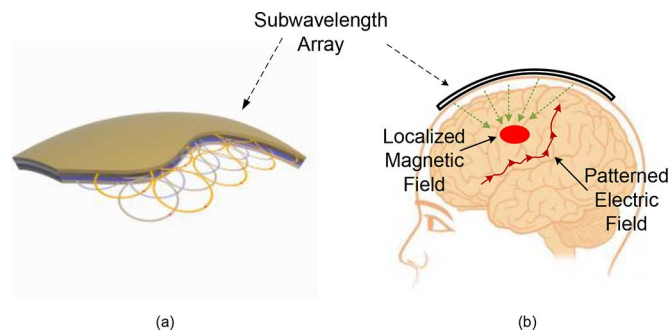
Fig. 1. Schematic of a possible application of the array for brain stimulation, and its basic working mechanism. (a) Curved array. (b) Application of the array.
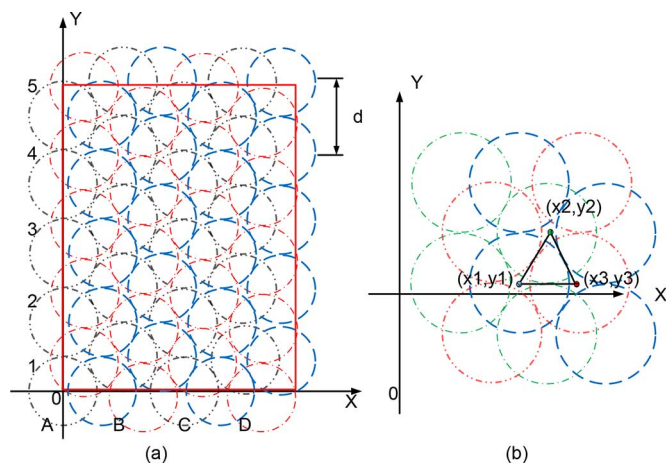

Fig. 2. Configuration of a three-layer subwavelength array. (a) Working area is marked by a rectangle and the number order of elements used in the synthesis process. (b) Relationship of adjacent elements on three different layers. The center points lead to an equilateral triangle.

stimulation (TMS), a method for stimulating excitable tissue with an electric field induced by an external time-varying magnetic field, can cause therapeutic effects in the brain [28]. This technique is used to treat neurological disorders such as depression. However, presently commercially available TMS systems using a pair of coils stimulate a region of the brain measuring roughly several centimeters. Seeking an effective way to precisely stimulate a small area inside the body is a significant challenge to existing biomedical devices.

In this paper, we present a new type of three-layer subwavelength coil array that enables us to pattern the magnetic field perpendicular to the array, as is shown in Fig. 1. The electric field or the electric current induced by the patterned magnetic field can then be precisely controlled, which may provide a new approach to biological applications of electromagnetics, such as brain stimulation or a brain/machine interface. A synthesis process for a 2-D pattern at an image plane for such a 2-D array is detailed, which allows us to easily obtain the asymmetrical patterned field in the near-field zone. The focusing performance of our proposed array is demonstrated numerically and experimentally and it is shown that the measured results are in good agreement with analytical and simulated results. Moreover, the presented structure can not only control the position of the focused electric field, but also its direction, which provides an additional degree of freedom. This may have the potential to improve the capabilities of noninvasive brain mapping systems [27], [29]. It is also found that the patterned magnetic field and focused electric field are in orthogonal planes. Using the proposed structure would allow for tissue stimulation in complex spatial patterns and rapid electronic scanning.

This paper is organized as follows. In Section II, a synthesis procedure to generate a desired electric-field pattern induced by a patterned magnetic field is discussed. A large matrix containing the near-field information of each element to each point in two dimensions is built, connecting the current on the coil to the near-field electric-field pattern. The least squares method with constraints is used to easily obtain the amplitude and the phase of excitation for each coil. In Section III, the presented array is examined through the proposed method and through full-wave simulations as a more effective and practical method for generating reconfigurable electric-field patterns. The design procedure for such a subwavelength array is reviewed, and the operation and design are verified through full-wave simulations. A sample of such a programmable three-layer subwavelength

array of 48 elements is fabricated and measured. All of the simulations in this paper are implemented by using Ansoft HFSS 15.0, a finite-element-method-based high-frequency structure simulation package.

II. DESIGN PROCEDURE

In this section, a subwavelength coil array for magnetic-field and electric-field pattern is presented and a detailed synthesis process is discussed, which could be extended to other near-field array applications.

Specifically, the design of the subwavelength array is based on the concept of sub-diffraction limit focusing and super-directive arrays, which can help us to focus electromagnetic fields to much smaller than what is currently possible. Fig. 2 illustrates the configuration of a three-layer subwavelength coil array in which the overlapped coils can produce a uniform magnetic-field distribution shown in the target area [30]. Similarly, the manipulation of the near field can also be achieved by controlling the excitation of each unit. The challenge to the design of such a structure is similar to that of super-directive antenna arrays [31], an approach where very dense arrays of antenna elements are used to achieve directivity in the far-field zone that is greater than what is dictated by the diffraction limit. Super-directive arrays have been built, but they typically suffer from high loss and low radiation resistance. The result is that they are difficult to impedance match, and the gain is reduced to such an extent that they are impractical for typical antenna applications such as communications or radar. Although these same challenges will exist for near-field subwavelength manipulation or focusing arrays, they will not result in practical limitations. First, such a subwavelength coil array is not designed for long-range communication, we do not need far-field radiation. Also, the efficiency is not an issue for some applications. If necessary, we can burn substantial power to deliver a few watts to the target area, which is just a few centimeters away. Furthermore, some TMS systems can use superconductive coils to minimize losses. Impedance matching is also less of an issue because the efficiency requirements are not as high as in wireless

communication and the operating frequencies in TMS systems up to few hundred MHz at most, where efficient matching circuits are easily designed. Furthermore, as suggested by Hansen [31], active circuits may be able to provide broadband matching for dense arrays. Considering these conditions, the problem is reduced to that of near-field pattern synthesis.

A. Synthesis Process

As shown in Fig. 3(a), an element, for example the nth coil, can produce an evanescent magnetic field perpendicular to the array. This characteristic can lead to an unattenuated magnetic-field penetration. The patterned magnetic field produces controlled electric field or current flow in the target area or the body tissue. Fig. 3(b) is a typical geometrical arrangement for loop antenna analysis, where a loop antenna is positioned symmetrically on the x–y-plane, at $z = 0$ [32]. In our research, the wire is assumed to be very thin, and the current spatial distribution is given as

$$I_\phi = I_0. \tag{1}$$

This type of current distribution is accurate enough due to the low operating frequencies and the loop having a very small circumference.

To find the near fields produced by this loop antenna, the potential function is given as

$$\vec{A}(x, y, z) = \frac{\mu}{4\pi} \int_c \vec{I}_e(x', y', z') \frac{e^{-jkR}}{R} dl'. \tag{2}$$

For the circular loop antenna, whose current is directed along a circular path, it would be more convenient to write the rectangular current components in terms of the cylindrical components. Then

$$\vec{I}_e = \vec{x}(I_\rho \cos \phi' - I_\phi \sin \phi')$$
$$+ \vec{y}(I_\rho \sin \phi' + I_\phi \cos \phi') + \vec{z}(I_z). \tag{3}$$

It should be emphasized that the source coordinates are designated as primed (ρ', ϕ', z') and the observation coordinates as unprimed (x, y, z). For the circular loop, the current is flowing in the ϕ direction so

$$\vec{I}_e = \vec{x}(-I_\phi \sin \phi') + \vec{y}(I_\phi \cos \phi'). \tag{4}$$

By referring to Fig. 3(b), the differential element length is given by

$$dl' = a d\phi'. \tag{5}$$

The potential function can then be written as

$$A_x = \frac{a\mu I_\phi}{4\pi} \int_0^{2\pi} - \sin \phi' \frac{e^{-jk|\vec{r} - \vec{r}'|}}{|\vec{r} - \vec{r}'|} d\phi' \tag{6a}$$

$$A_y = \frac{a\mu I_\phi}{4\pi} \int_0^{2\pi} \cos \phi' \frac{e^{-jk|\vec{r} - \vec{r}'|}}{|\vec{r} - \vec{r}'|} d\phi'. \tag{6b}$$

Assuming the operating frequency can be up to 100 MHz, the wavenumber $k = (2\pi)/(\pi) = (2\pi)/(3000) = 2 \times 10^{-3}$
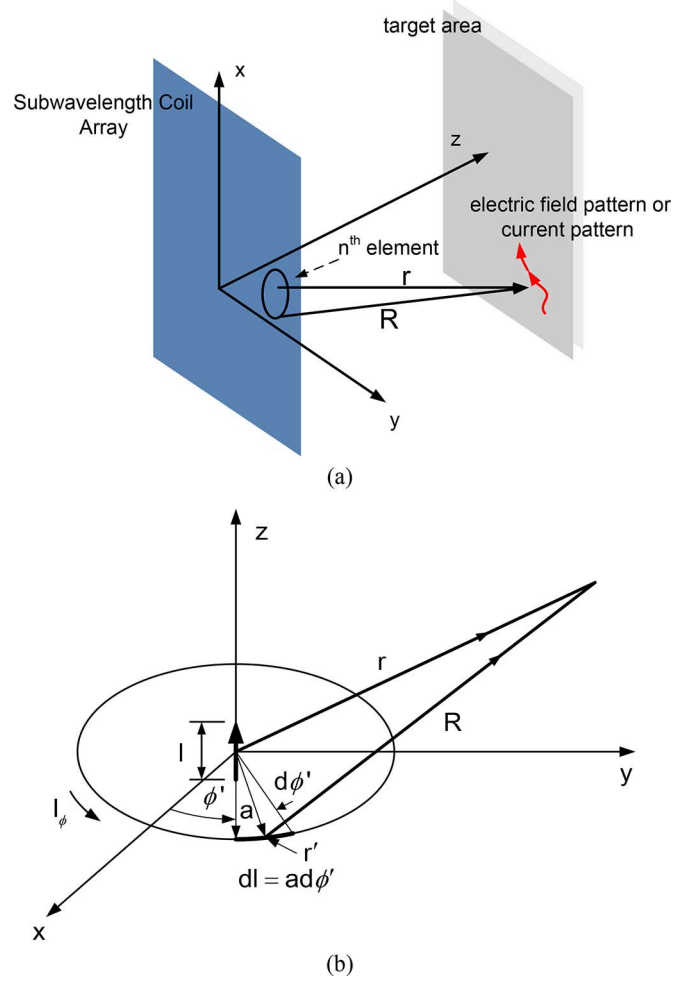

(a)

(b)

Fig. 3. Illustration of a subwavelength coil array for the near-field synthesis. (a) Subwavelength coil array ($z = 0$) produces near-field excitation to provide coverage at a target area, where an element is extracted and related position vectors are also indicated. (b) Geometrical arrangement for an element analysis.

rad/mm. Since the area of interest is about 3 cm [26], the exponential function $e^{-jk|\vec{r} - \vec{r}'|} \approx 1$. Thus, the potential function reduces to

$$A = \vec{x}\frac{a\mu I_\phi}{4\pi} \int_0^{2\pi} - \sin \phi' \frac{1}{|\vec{r} - \vec{r}'|} d\phi' + \vec{y}\frac{a\mu I_\phi}{4\pi}$$
$$\times \int_0^{2\pi} \cos \phi' \frac{1}{|\vec{r} - \vec{r}'|} d\phi'. \tag{7}$$

The magnetic field can then be obtained from the potential function definition

$$\nabla \times \vec{A} = \mu \vec{H}. \tag{8}$$

In the application of TMS systems, the electric field or the current induced by the magnetic field is the component of the electromagnetic field, which produces effects on the neurons. From Maxwell's equations, we can obtain the induced current or electric field given by (9) as follows:

$$\nabla \times \vec{H} = \vec{J} + \frac{\partial \vec{D}}{\partial t}. \tag{9}$$

As is known, the human brain can be treated as a conductor [27], where the conduction current is dominant over the displacement current. The conduction current is governed by Ohm's law,

$$\vec{J} = \sigma \vec{E} \qquad (10)$$

where σ (S/m) is the conductivity. Hence, the induced electric-field profile in the target area can be expressed as

$$\vec{E}(x, y) = \frac{1}{\sigma \mu} (\nabla \times (\nabla \times \vec{A})). \qquad (11)$$

The analytical formulation for the electric-field pattern by a coil can be extended to a 2-D three-layer array with an arbitrary number of elements. The total 2-D electric field for an array of N elements is given by (12)

$$\vec{E}(x, y) = \sum_{n=1}^{N} \frac{a I_n}{4\pi\sigma} \left(\nabla \times \left(\nabla \times \left(\vec{x} \int_0^{2\pi} \frac{-\sin\phi'}{|\vec{r} - \vec{r}_n'|} d\phi' \right. \right. \right.$$
$$\left. \left. \left. + \vec{y} \int_0^{2\pi} \frac{\cos\phi'}{|\vec{r} - \vec{r}_n'|} d\phi' \right) \right) \right)$$
$$= \sum_{n=1}^{N} I_n \vec{M}_{(x,y),n} = \vec{M}_{(x,y)} \cdot I \qquad (12)$$

where I_n represents the input current on the nth coil. I is an N-element column vector containing the feeding information assigned to each coil and $\vec{M}$ is an N-element row vector representing the electric field from each coil as a function of (x, y). The magnitude and phase of I_n can be obtained for each individual coil to produce the desired electric-field profile $\vec{E}(x, y)$. In order to determine the optimal feeding current I_{opt} on each coil to approximate a desired electric-field profile $\vec{f}(x, y)$ in the target area, each coil feeding component can be regarded as a basis function for a method of moments field expansion. By multiplying both sides $\vec{f}(x, y) \approx \vec{M}_{x,y} \cdot I_{\mathrm{opt}}$ by $\vec{M}^*_{(x,y),m}$ and integrating over (x, y), we can obtain a system of N independent equations that can be solved for N feeding currents I_n by reducing the problem to that of inverting an $N \times N$ matrix. Although these basis functions are linearly independent, they are not orthogonal so the off-diagonal elements of the matrix do not vanish and the analytical formulation becomes unwieldy [6]. Another challenge to solving these equations is the integration as a function of ϕ' in the denominator, which, for a very thin circular loop of any radius, can be carried out and is represented by a complex infinite series whose real part contains complete elliptic integrals of the first and second kind, while the imaginary part consists of elementary functions. This treatment is only valid provided the observation distance is greater than the radius of the loop ($r > a$) [32], [33]. Although the loop used in our research is very small, the observation is also in the near-field zone from which the distance may be smaller than the radius of the loop. Another very detailed and systematic treatment is that of [34] and [35], which is valid for any observation distance, except when the observation point is on the loop itself. However, these methods are very complex in practice [32].

Here, we build a matrix bridging between the feeding current and patterned electric-field profile represented as $\vec{M}'_{(x,y)} = M_x + i M_y$. $\vec{f}(x, y)$ and $\vec{M}_{(x,y)}$ can then be expressed as a column vector by discretizing them over (x, y), and stored as
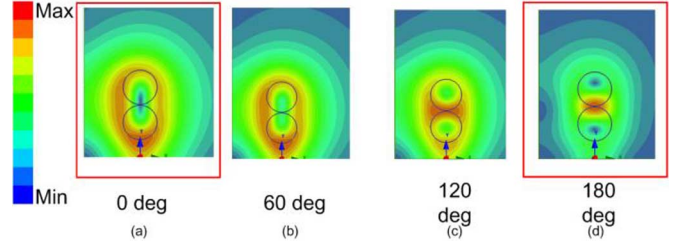

Fig. 4. Variation of field pattern $|E|(x, y, z)$ along with the change of phase difference between two adjacent elements. Phase difference is: (a) $0°$, (b) $60°$, (c) $120°$, and (d) $180°$.

one dimension, thus reducing the method of moments to the method of least squares [36]. Therefore, the induced electric-field pattern in the brain can be expressed by input currents on the coils given by (13). In the matrix $\vec{M}'_{(x,y)}$, the real part represents the x component and the imaginary part represents the y component, which can be used for the curl operation. Different from 1-D or symmetrical near-field pattern synthesis [6], [22], this method simplifies the complicated pattern synthesis by just solving one equation,

$$\vec{E}(x, y) = \sum_{n=1}^{N} \frac{a I_n}{4\pi\sigma} \left(\nabla \times \left(\nabla \times \left(\vec{x} \int_0^{2\pi} \frac{-\sin\phi'}{|\vec{r} - \vec{r}'|} d\phi' \right. \right. \right.$$
$$\left. \left. \left. + i\vec{y} \int_0^{2\pi} \frac{\cos\phi'}{|\vec{r} - \vec{r}_n'|} d\phi' \right) \right) \right)$$
$$= \sum_{m=1}^{N_x \times N_y} \sum_{n=1}^{N} I_n \vec{M}'_{(x,y),mn} = \vec{M}'_{(x,y)} \cdot I. \qquad (13)$$

It is noted that the ease of this synthesis method makes the imaginary part of obtained current excitation physically meaningless. In this design, the element is electrically small and the current distribution on coils can be treated as constant for convenience. For practical purposes, the phase of the currents in each element can be taken to be either in-phase or out-of-phase such that the field profile is stationary with time. This assumption can be vindicated from Fig. 4, where the near-field pattern per cycle produced by in-phase excitations is similar to that by excitations with $60°$ phase difference and pattern per cycle by out-of-phase excitations similar to that by $120°$ phase-difference excitations. Otherwise, if the phase difference is chosen to be the values between $0°$ to $180°$, the magnetic fields produced by adjacent coils vary in magnitude and in direction out of step along with time within one cycle. In this case, the different parts of the patterned electric-field profile would be focused asynchronously. Hence, the phases of excitation can be only either in-phase or out-of-phase, and the patterned electric-field profile is time-invariant in position and polarization. Thus, (13) is expressed as a complex matrix as (14), then we can extract the real part and imaginary part of the obtained input current on each coil,

$$(E_r + j E_i) = (M_r + j M_i) \times (I_r + j I_i). \qquad (14)$$

In order to eliminate the meaningless imaginary parts of the excitation matrix and to ensure a solution for a excitation under in-phase or out-of-phase condition, we rephrase (14) as (15)

with a constraint condition given by (16), where $0_{n,n}$ represents $N \times N$ zero matrix and $I_{n,n}$ is $N \times N$ identity matrix,

$$\begin{bmatrix} E_r \\ E_i \end{bmatrix} = \begin{bmatrix} M_r & -M_i \\ M_i & M_r \end{bmatrix} [I] \qquad (15)$$

$$[0_{n,n}, I_{n,n}][I] = 0_{n,n}. \qquad (16)$$

From the above discussion, it is now easy to pattern the electric-field profiles in controlled polarization at multiple areas in the near-field zone. The polarization of the focused electric field can also be determined by adjusting the weights of the x or y component of the target function. If the area of interest is in a further distance or the operating frequency is high enough where $e^{-jk|\vec{r}-\vec{r}|} \approx 1$ is not valid any more, a more complicated optimization based on the equal or unequal weights for x and y component matrices can be acquired using the same idea.

B. Mutual Impedance

In the synthesis process mentioned above, each near-field pattern used for the expansion of the target distributions is created by exciting a different element while short circuiting the other loop elements. It is noted that the actual element can be properly excited by multiplying the synthesized optimal weights with an impedance matrix that accounts for the mutual coupling effects among elements as addressed in the method of moments [22]. The mutual impedance among elements in our research is primarily due to inductive coupling where the coupling currents have a phase shift of $\pm 90°$, which can be known through circuit equivalence or extracted from numerical software.

The relationship between the terminal voltage of any one element in terms of currents flowing in the others can be written as [32]

$$V_{mn} = \sum_p \sum_q Z_{mn,pq} I_{pq} \qquad (17)$$

where V_{mn} defines the terminal voltage at element mn due to a unity current in element pq when the current in all other elements is zero. Thus, the $Z_{mn,pq}$ terms represent the mutual impedance when indices mn and pq are not identical. Here, the mutual impedance matrix is obtained through simulation by Ansoft HFSS, in which the mutual impedance $Z(\omega)$ can be obtained as an $N \times N$ matrix, where N represents the number of elements. Thus, (17) can be expressed as

$$V_d = Z(\omega)I_f = [Z_{n,n}(\omega)]I_d \qquad (18)$$

in which V_d is the desired terminal voltage of the elements and I_f is the actual feeding current on the elements. I_d is the desired terminal current of the elements, which can be obtained by the proposed synthesis method. Thus, the feeding current for the elements can be obtained through

$$I_f = Z(\omega)^{-1}[Z_{n,n}(\omega)]I_d. \qquad (19)$$

Now let us consider the synthesis of a near-field pattern based on our presented structure.

TABLE I
DESIRED CURRENTS OF COILS ON THE FIRST LAYER

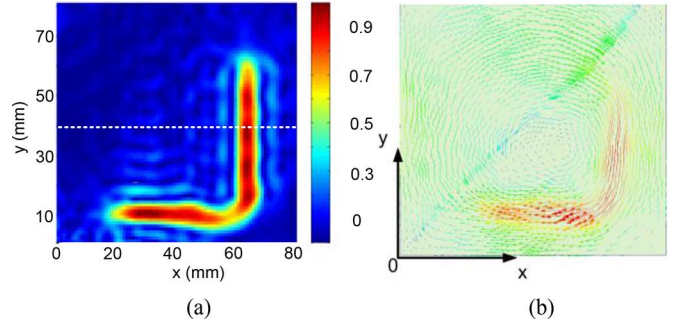|	A	B	C	D
1	0.005	-0.009	1	0.018
2	-0.000	0	-0.153	0.099
3	-0.007	-0.002	0.000	0.115
4	-0.000	0.001	0.004	-0.006

Fig. 5. (a) Analytical and (b) simulated focused electric-field pattern at the 2-D target area 3 mm below subwavelength array.

III. SUBWAVELENGTH ARRAY

A. Configuration and Synthesis

A subwavelength coil array of 48 units and 4×4 coils on each layer is analyzed, as shown in Fig. 2. Each coil has a radius of 12 mm, and element separation $d = 24.3$ mm. The thickness of each layer is 0.2 mm in the full-wave simulation. A box full of sea water below the presented array resembles brain tissue and is also the target area for focusing electric-field patterns. The optimal weights for each coil were calculated using the method discussed above for a right angle bent electric-field profile. We chose this field profile as an example to illustrate that our array can produce polarized patterns. Table I shows the normalized excitations for coils on the first layer, where it is noted that the coils are just in-phase or out-of-phase. As mentioned in Section II, for an electric-field pattern, it can be regarded as the combination of x-component fields and y-component fields, each of which are formed through the fields produced by several elements. Controlling each component can define the polarization of the electric field. From that, the polarized arbitrary field pattern can be obtained in which the field direction is along the focused field pattern. The mutual impedance matrices at operating frequencies are then obtained to mitigate the coupling effects due to the dense arrangement. Each magnitude of the excitations can be scaled to any value, which can be used to adjust the magnetic-field intensity the coils produce without affecting the desired focusing pattern. Plotted in Fig. 5 are the analytical and full-wave simulated 2-D patterned electric-field profiles. Although the analytical method is approximate, it is still accurate in our research due to the target area being very close to the array. The direction of the electric field is along the patterned line, as shown in Fig. 5(b). The electric field in the near-field zone is simulated at 1 MHz, and its normalized magnitude sampled along the slice at 3 mm away from the subwavelength array that is indicated by dashed line in Fig. 5(a) is plotted compared
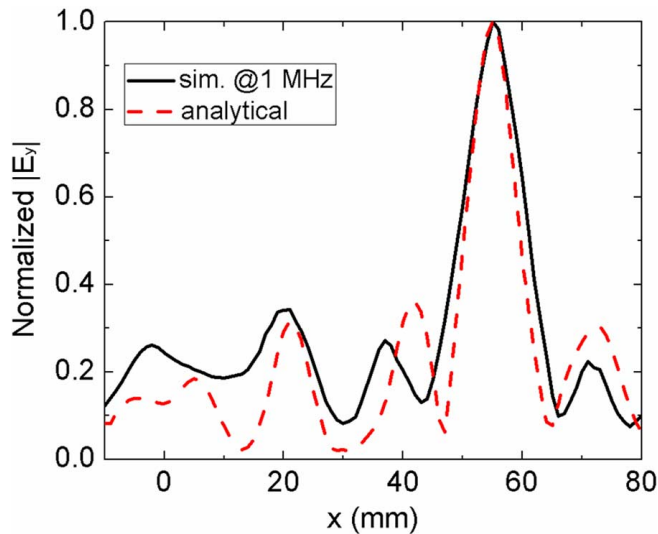
Fig. 6. Comparison of simulated and analytical results. Normalized magnitude of analytical and simulated y-polarized electric-field components sampled along the line $y = 40$ mm indicated in Fig. 5(a).

Fig. 7. Effects of coil size. Variation of beamwidth of y-polarized electric-field component with the element size sampled along the line $y = 40$ mm indicated in Fig. 5(a).

with the analytical result, as is shown in Fig. 6. A slight discrepancy is seen between the analytical and simulated results, which is primarily from the phase errors produced in the approximation given by $e^{-jk|\vec{r}-\vec{r}'|} \approx 1$. It is evident that this discrepancy is mainly in the suppressed area but does not affect the contrast between the focused fields and suppressed fields.

From the simulation results, it is found that the half-power beamwidth is 8 mm at 1 MHz. It is desirable and expected to have a higher resolution if the elements are smaller. Another larger array of 192 coils, which have radii of 6 mm, is simulated in the same configuration, and the same right angle bent electric-field profile is generated. The analytical comparison between the normalized electric-field magnitudes focused by these two arrays sampled along the dashed line indicated in Fig. 5(a) is plotted in Fig. 7. It is expected that the focusing resolution is improved and the focused half-power beamwidth is reduced. The electric field outside the target region is strongly suppressed due to the increased control of the field pattern enabled by the larger number of elements. Note also that increasing the number of elements and diminution of each element in size does not significantly decrease the width of the beam produced, which is already very narrow.

The electric field produced by one element is shown in Fig. 8, where the electric field diverges very quickly. It is found that the electric field is significantly more diffuse at 9 mm away from the element. The normalized focused electric field acquired in the slice in Fig. 5(a) along with various distances from the array at different frequencies are depicted in Fig. 9. The electric field is normalized to the peak value at each slice for comparison. It is evident that the sidelobe levels of focused electric field at 100 kHz are a little higher than that at higher frequencies, especially at the target planes far from the subwavelength array. It is also found that the focused beamwidth is decreased as the operating frequency increases, i.e., 10 mm at 100 kHz and 7.5 mm at 100 MHz sampled at the target plane 3 mm below the array. The nondiffractive range where the electric field is focused is
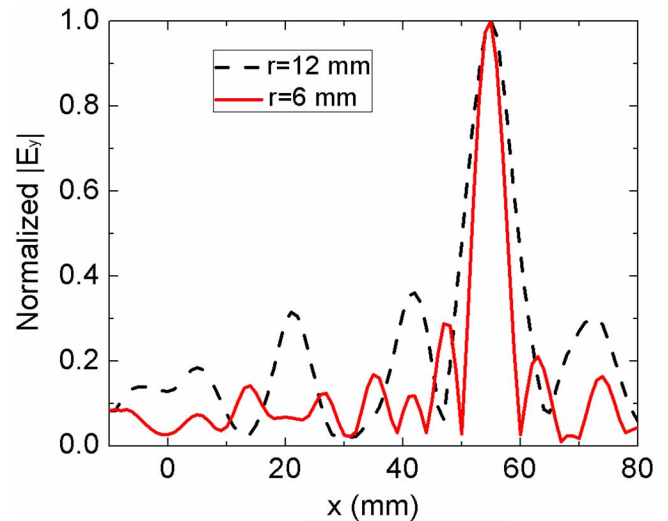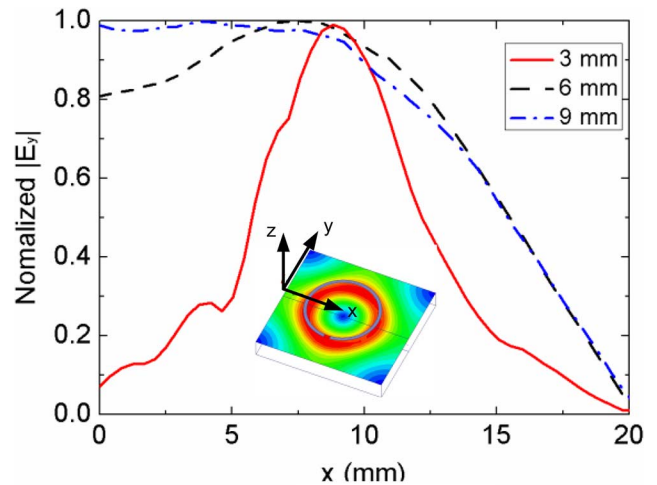

Fig. 8. Electric fields generated by the single coil. Normalized magnitude of simulated electric field acquired at $y = 0$ mm along the x-axis at various distances away from the element.

30 mm at 100 kHz and 32 mm at 100 MHz. The nondiffractive range is almost the range the near fields produced by the array element die out, as indicated in [14].

B. Experimental Results

A subwavelength array including 48 elements is fabricated and measured in this section to demonstrate the implementation of the proposed method. Here, each element is a loop with radius of 12 mm equivalent to that in the simulation. A small gap of 2 mm on each coil is used as the feeding point for driving the loop. A ground plane between the array and the bottom layer is also present for isolating the near field from affecting the feeding network on the back of the board. It should be noted that the ground plane has a limited effect on the synthesized near-field pattern due to the radiationless property of proposed structure even though the ground is placed very close to the array. From the simulated results, a 4-mm gap is enough as
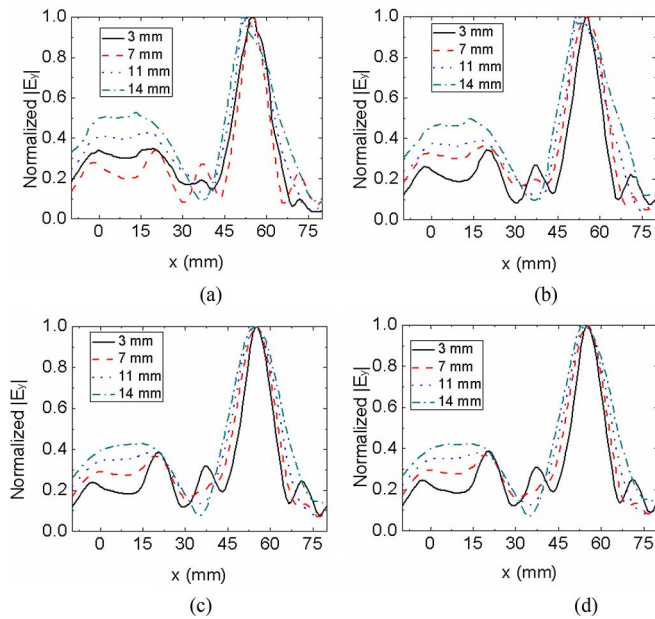
Fig. 9. Normalized magnitude of simulated focused y-polarized electric field acquired in the slice shown in Fig. 5(a) at various distances away from the subwavelength array. (a)100 kHz. (b) 1 MHz. (c)10 MHz. (d)100 MHz.
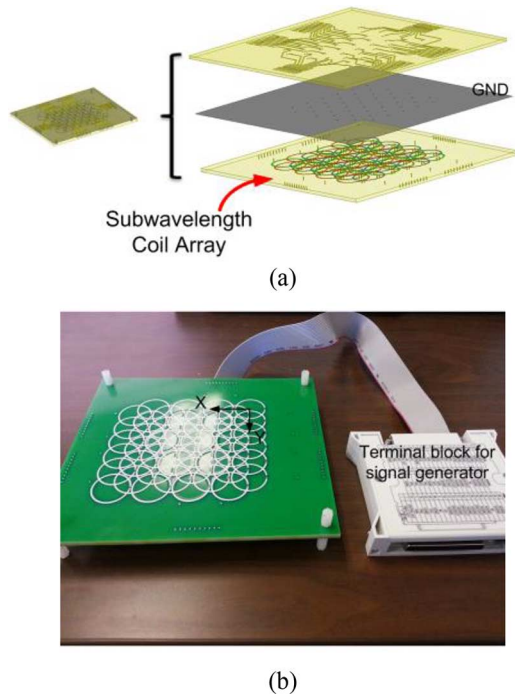

Fig. 10. Fabricated subwavelength array. (a) Configuration of fabrication. (b) Fabricated subwavelength array, where the silk screen shows the positions of elements. The coordinate in the figure is used for measurement.

the separation between the subwavelength array and the ground plane for a nondistorted electric-field pattern. Six high-speed ribbon cables are responsible for connecting the feeding network and the signal terminal blocks of the signal generator, as shown in Fig. 10.
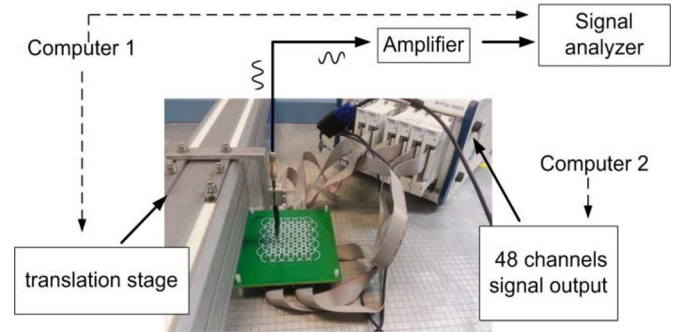

Fig. 11. Measurement system for 2-D near-field scanning. The probe in the figure is used to acquire the magnetic field.
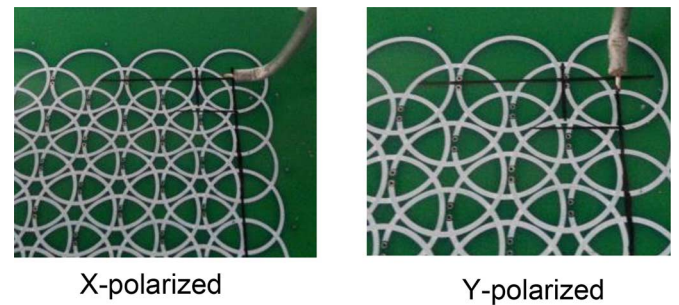

Fig. 12. Electric-field probe for each polarization.

The measurement system is illustrated in Fig. 11, where the signals are produced by six PXI-6733 cards from National Instruments (NI). A small loop as a magnetic-field probe and a small monopole for electric-field acquisition are used to scan the near-field controlled by an automated 2-D translation stage. The signal received by the probe is analyzed by a signal analyzer. The signal generator, translation stage, and the signal analyzer are all controlled by using NI Labview software, which is also used for the near-field scanner and data acquisition. The near field was measured over an area 80 mm × 80 mm with a step of 1 mm, and the measurement coordinates are depicted in Fig. 10. Since the patterned electric fields can be determined as the desired polarization, polarized probes are required to acquire the corresponding polarized electric fields, which is important for advanced neuron stimulation [27]. Similar to the radiation mechanism of a monopole, Fig. 12 shows the deployment of the electric-field probe in x polarization and y polarization. The feeding current on each element is obtained using the method described above, and then scaled to appropriate values to make sure the output currents are not distorted. A right-angle bent-shape electric-field profile is initially patterned as shown in Fig. 5 and measured at 0.1 MHz. The electric field is measured in sea water resembling brain tissues, where the electric-field probes used are shown in Fig. 12. An x-polarized probe can receive the focused electric field in x polarization and a y-polarized probe is for the electric-field measurement in y polarization. The measured electric field along the xy-plane and a complete 2-D scan at 3 mm away from the subwavelength array for a right-angle bent-shape pattern are given in Fig. 13. It is
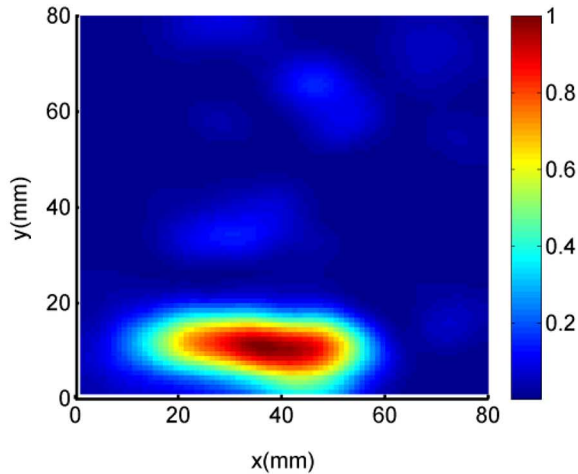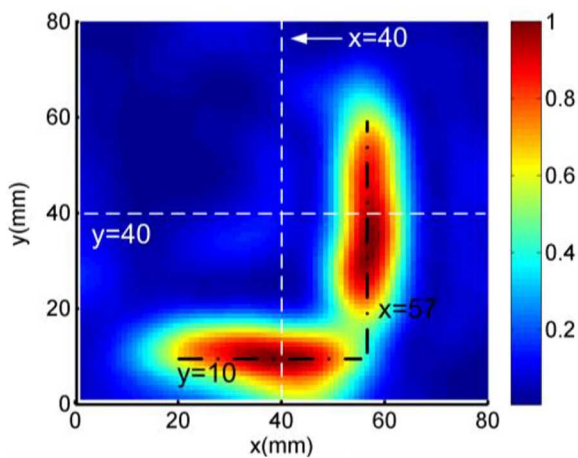
(a)
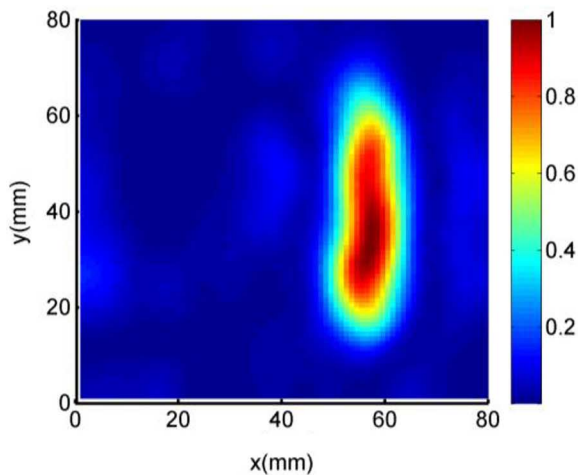
(b)

(c)

Fig. 13. Normalized magnitude of measured electric-field energy for right angle bent profile. (a) 2-D measured electric field probed by x-polarized monopole. (b) 2-D measured electric field probed by y-polarized monopole. (c) The combined measured near-field pattern through vector superposition. Dotted lines represent the patterned electric fields with the direction along the line. Dashed lines are the sampled lines for focusing effects.

evident from this figure that the electric field in the near-field zone is correctly polarized and each field component in one direction can only be measured by a corresponding polarized
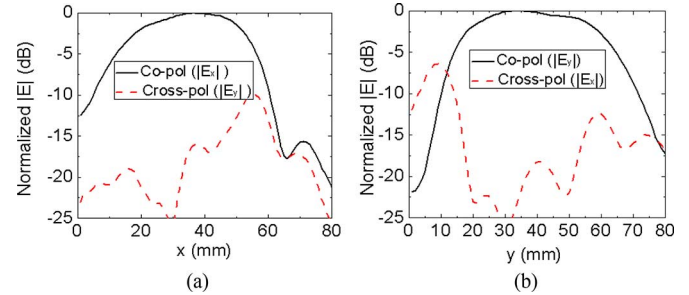

Fig. 14. Patterned electric field along the interested direction. Normalized magnitude of measured electric field in co-polarization and cross-polarization. (a) Normalized magnitude of measured x-polarized electric field along $y = 10$ mm (dotted line), as shown in Fig. 13. (b) Normalized magnitude of measured y-polarized electric field along $x = 57$ mm (dotted line), as shown in Fig. 13.

electric-field probe. Fig. 13(c) gives the combination of measured x-polarized and y-polarized electric field through vector superposition. It should be noted that this combination is undertaken under the assumption that the measured field is ideally polarized. From 13(c), the measured electric-field profile clearly confirms the desired near-field pattern represented by the dotted line. It is also found that the measured electric-field value at the emerging area is about 0.6 of the peak value, which agrees very well with the synthesized result shown in Fig. 5(a).

The polarization term in antenna designs is employed to study the ability of the proposed array to control the direction of patterned electric fields. Here, the co-polarized electric field is the electric field in the intended direction, and the cross-polarized electric field is the electric field in the orthogonal direction. Fig. 14 gives the magnitude of the measured electric fields in the co-polarization and cross-polarization in decibels for each directed focused electric-field profile shown by the dotted line in Fig. 13(c). It is noted that the magnitude of the electric field in the cross-polarization is about 20 dB lower than that in co-polarization, except the x-polarized electric field ranging from $x = 40$ mm to $x = 60$ mm where the x-polarized field merges to the y-polarized field. Similarly, the large cross-polarized electric-field intensity in the y-polarized field pattern when $y = 10$ mm to $y = 20$ mm can be found.

In order to study the focused beamwidth, the co-polarized electric field across the focused area is measured and plotted in Fig. 15. It is found that the focused half-power beamwidth is 11 and 10 mm in Fig. 15(a) and (b), respectively, which were within 10% deviation from the simulated value of 10 mm. This error is in line with the expectation because the electric-field probe is 1 mm in diameter in itself.

IV. RECONFIGURABILITY OF NEAR-FIELD PATTERN

Using an L-shaped electric-field profile, the synthesis process has been demonstrated in both simulation and experiment. If the data in matrix M' is obtained in advance and stored, it is convenient to adjust the electric-field profile by programming the exciting sources using the least squares method without computing the near-field distribution from each element again. Our Labview code allows the signal generator to read the excitation information obtained directly. Thus, the presented method can
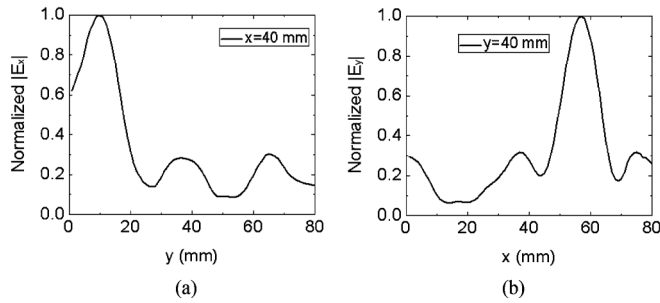
Fig. 15. Focusing effects of co-polarized electric fields. Normalized magnitude of measured electric field based on the coordinate of Fig. 13(c). (a) Normalized magnitude of measured x-polarized electric field along the line $x = 40$ mm (dashed line). (b) Normalized magnitude of measured y-polarized electric field along the line $y = 40$ mm (dashed line).

allow us to quickly pattern various electric-field profiles. Previously, the x-polarized field and y-polarized field is patterned individually to form a right angle bent electric-field profile. Here, a line shape electric-field profile inclined at $45°$ to the x-axis, which consists of x-polarized field and y-polarized field equally is quickly patterned and measured. The electric-field pattern in co-polarization is acquired by the electric-field probe rotated by $45°$ from the x-axis. Fig. 16(a) plots the measured complete 2-D normalized electric-field profile in co-polarization 3 mm away from the subwavelength array. It is evident that an inclined electrical pattern is shaped as is expected, which indicates the validation and flexibility of our proposed method. The electric field in the cross-polarization normalized to the peak value in the co-polarization is also shown in Fig. 16(b). It is found from the scale that the maximum field energy in the cross-polarization is 0.22 of that in the co-polarization.

Similarly, the focused electric-field magnitudes in co-polarization and in cross-polarization are also illustrated in Fig. 17. The electric-field power in cross-polarization is about 10 dB lower, which is higher than that in the right-angle bent-shape pattern. This can be attributed to the relatively sparse arrangement of the elements for this profile, which makes the patterned electric fields in twists. Under this circumstance, the focused electric field in co-polarization is deteriorated and in the cross-polarization is increased. The twists in current direction also lead to ripples in the cross-polarized field. This also can be seen through the measured magnetic fields plotted in Fig. 18, where the uneven magnetic-field distribution along the patterned electric-field profile results in a twisted electric field. It is also found that the magnetic fields gradually fade with the distance from the target area and approach zero at long distances.

The measured z-directed electric fields normalized to the peak value of the focused electric field in co-polarization are plotted in Fig. 19. It is evident that the focused electric fields are confined in the xy-plane where the z-directed electric-field peak value is only three-thousandths of the focused electric fields in the xy-plane.

In order to study the focused beamwidth, the focused electric field in the co-polarization along the sampled line $y = -x + 40$, shown in Fig. 16, is depicted in Fig. 20. It is worth noting that the focused half-power beamwidth is 10 mm, similar to that
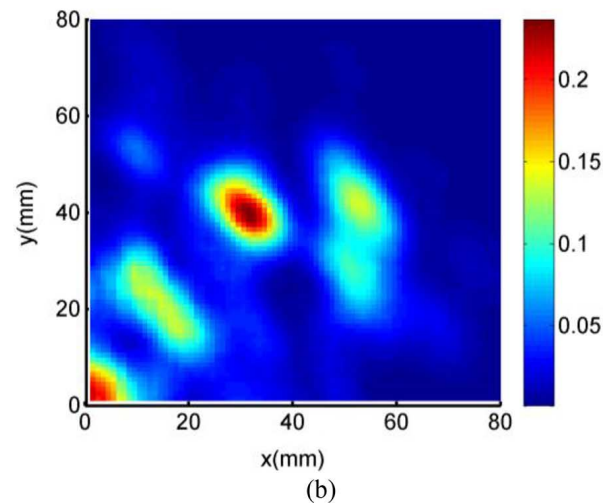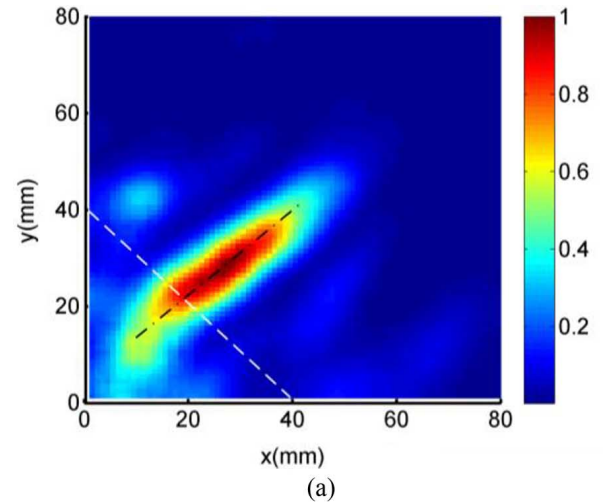

Fig. 16. Normalized magnitude of measured electric field for a $45°$ inclined-line profile. (a) Normalized magnitude of measured electric field in co-polarization. The dotted line represents the patterned electric fields with the direction along the line. The dashed line is the sampled line for focusing effects. (b) Measured electric field in cross-polarization normalized to the peak value in co-polarization.
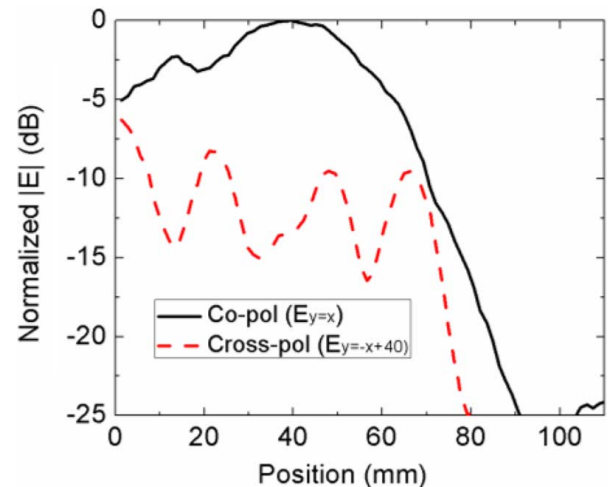

Fig. 17. Patterned electric field along the interested direction. Normalized magnitude of measured electric field in co-polarization and cross-polarization acquired along the line $y = x$ (dotted line) in Fig. 16.
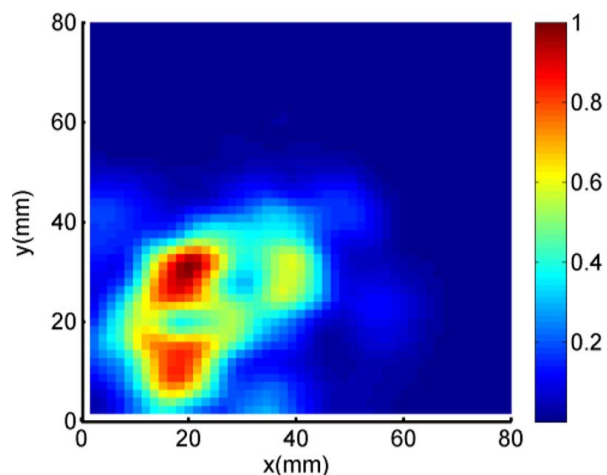
Fig. 18. Normalized magnitude of measured magnetic field that leads to the inclined 45° electric-field line profile.

Fig. 20. Focusing effects of co-polarized electric fields. Normalized magnitude of measured electric field acquired along the line $y = -x + 40$ (dashed line) [see Fig. 16(a)].

and electric-field patterns in a 2-D image plane. In this paper, a right-angle bent profile and an inclined-line electric-field profile, which indicate the x-polarized component and y-polarized component unequally and equally, are successfully patterned. A three-layer subwavelength array of 48 elements is fabricated and measured based on a 2-D near-field scanning measurement system controlled by Labview software. The magnetic field and electric field including polarization are acquired by a small loop and a polarized small monopole, respectively. It is shown that measured results agree very well with the synthesized ones and the desired electric-field profile can be patterned symmetrically and asymmetrically in terms of position and polarization.

This work can extend to several possible future research scenarios. First, the synthesis method presented above shows that 2-D magnetic fields and electric fields desired at an image plane in the near-field zone can be easily obtained by just solving one matrix. This method can be used for other near-field subwavelength focusing synthesis where the target area is close to the array and unit cells are electrically small, which are exactly the case for most near-field applications. The magnetic-field pattern and focusing array such as the one presented here may find applications in enhanced performance electric actuators that are based on the focused magnetic fields [12], [13], and in the wireless power transfer by controlling the near-field patterns [23], [30]. Another possible future application, which is the primary motivation for this research, is generating patterned electric fields inside tissues for neural stimulation.

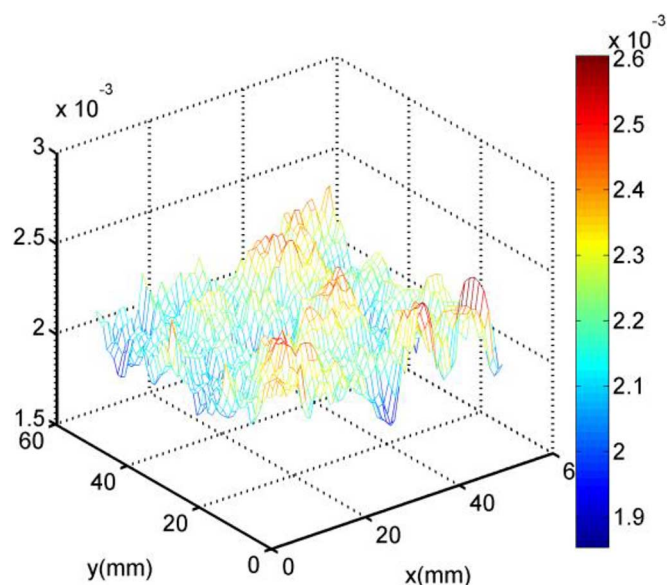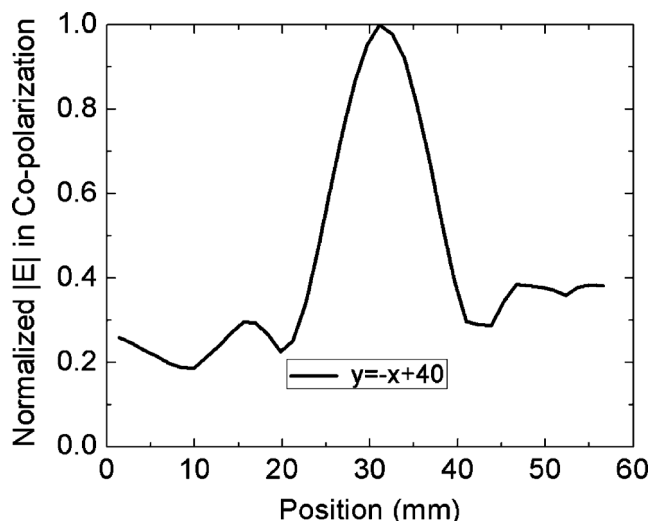Fig. 19. Measured profile of z-directed electric field normalized to the peak value of focused electric field in co-polarization for the inclined 45° electric-field line profile.

in the right-angle bent pattern, which indicates the invariable beamwidth without being affected by the change of pattern.

V. CONCLUSION

It has been found that a 2-D array of electrically small loops with subwavelength spacing, designed borrowing the concepts of super-directive antenna arrays and the sub-diffractive focusing limit, can be used for various subwavelength focused magnetic-field and electric-field patterns on an image plane set in the near-field zone. A detailed synthesis method based on the least square optimization with constraint condition is discussed, which allows one to expedite various patterns formed with a near-field information matrix computed and stored in advance. The presented method is based on an acceptable approximation, which simplifies the optimization process by generating x and y component matrices and combining them to a single one. It can be used to design a wide variety of desired focused magnetic-

REFERENCES

[1] E. Synge, "XXXVIII. A suggested method for extending microscopic resolution into the ultra-microscopic region," *Phil. Mag.*, vol. 6, no. 35, pp. 356–362, 1928.

[2] D. Pohl, W. Denk, and M. Lanz, "Optical stethoscopy: Image recording with resolution $\lambda/20$," *Appl. Phys. Lett.*, vol. 44, no. 7, pp. 651–653, Apr. 1984.

[3] E. Ash and G. Nicholls, "Super-resolution aperture scanning microscope," *Nature*, vol. 237, pp. 510–513, Jun. 1972.

[4] J. B. Pendry, "Negative refraction makes a perfect lens," *Phys. Rev. Lett.*, vol. 85, no. 18, pp. 3966–3969, Oct. 2000.

[5] L. Verslegers, P. B. Catrysse, Z. Yu, and S. Fan, "Deep-subwavelength focusing and steering of light in an aperiodic metallic waveguide array," *Phys. Rev. Lett.*, vol. 103, no. 3, pp. 033902–033902-4, Jul. 2009.

[6] L. Markley, A. M. Wong, Y. Wang, and G. V. Eleftheriades, "Spatially shifted beam approach to subwavelength focusing," *Phys. Rev. Lett.*, vol. 101, no. 11, pp. 113901–113904, Sep. 2008.

[7] A. Sentenac and P. C. Chaumet, "Subdiffraction light focusing on a grating substrate," *Phys. Rev. Lett.*, vol. 101, no. 1, pp. 013901–013904, Jul. 2008.

[8] R. Merlin, "Radiationless electromagnetic interference: Evanescent-field lenses and perfect focusing," *Science*, vol. 317, no. 5840, pp. 927–929, Jul. 2007.

[9] A. Grbic, L. Jiang, and R. Merlin, "Near-field plates: Subdiffraction focusing with patterned surfaces," *Science*, vol. 320, no. 5875, pp. 511–513, Oct. 2008.

[10] A. Grbic, R. Merlin, E. M. Thomas, and M. F. Imani, "Near-field plates: Metamaterial surfaces/arrays for subwavelength focusing and probing," *Proc. IEEE*, vol. 99, no. 10, pp. 1806–1815, Oct. 2011.

[11] M. F. Imani and A. Grbic, "An experimental concentric near-field plate," *IEEE Trans. Microw. Theory Techn.*, vol. 58, no. 12, pp. 3982–3988, Dec. 2010.

[12] D. Banerjee, J. Lee, E. M. Dede, and H. Iizuka, "Kilohertz magnetic field focusing in a pair of metallic periodic-ladder structures," *Appl. Phys. Lett.*, vol. 99, no. 9, pp. 093501–093501-3, Aug. 2011.

[13] E. M. Dede, J. Lee, Y. Guo, L. Q. Zhou, M. Zhang, and D. Banerjee, "Kilohertz magnetic field focusing and force enhancement using a metallic loop array," *Appl. Phys. Lett.*, vol. 101, no. 2, pp. 023506–023509, Jul. 2012.

[14] F. Gao, F. Zhang, M. Huang, and D. F. Sievenpiper, "Programmable screen for patterning magnetic fields," *IEEE Trans. Microw. Theory Techn.*, vol. 62, no. 3, pp. 481–490, Mar. 2014.

[15] K. Finkenzeller and R. Waddington, *RFID Handbook: Radio-Frequency Identification Fundamentals and Applications*. New York, NY, USA: Wiley, 1999.

[16] H.-T. Chou, T.-M. Hung, N.-N. Wang, H.-H. Chou, C. Tung, and P. Nepa, "Design of a near-field focused reflectarray antenna for 2.4 GHz RFID reader applications," *IEEE Trans. Antennas Propag.*, vol. 59, no. 3, pp. 1013–1018, Mar. 2011.

[17] R. Gadh, G. Roussos, K. Michael, G. Q. Huang, B. S. Prabhu, and P. Chu, "RFID-a unique radio innovation for the 21st century," *Proc. IEEE (Special Issue)*, vol. 98, no. 9, pp. 1546–1549, Sep. 2010.

[18] K. S. Rao, P. V. Nikitin, and S. F. Lam, "Antenna design for UHF RFID tags: A review and a practical application," *IEEE Trans. Antennas Propag.*, vol. 53, no. 12, pp. 3870–3876, Dec. 2005.

[19] K. Stephan, J. Mead, D. Pozar, L. Wang, and J. Pearce, "A near field focused microstrip array for a radiometric temperature sensor," *IEEE Trans. Antennas Propag.*, vol. 55, no. 4, pp. 1199–1203, Apr. 2007.

[20] J. Lin and C. Li, "Wireless non-contact detection of heartbeat and respiration using low-power microwave radar sensor," in *Asia–Pacific Microw. Conf.*, 2007, pp. 1–4.

[21] H.-T. Chou, K.-L. Hung, and H.-H. Chou, "Design of periodic antenna arrays with the excitation phases synthesized for optimum near-field patterns via steepest descent method," *IEEE Trans. Antennas Propag.*, vol. 59, no. 11, pp. 4342–4345, Nov. 2011.

[22] H.-T. Chou, N.-N. Wang, H.-H. Chou, and J.-H. Qiu, "An effective synthesis of planar array antennas for producing near-field contoured patterns," *IEEE Trans. Antennas Propag.*, vol. 59, no. 9, pp. 3224–3233, Sep. 2011.

[23] A. Ludwig, C. D. Sarris, and G. V. Eleftheriades, "Near-field antenna arrays for steerable sub-wavelength magnetic-field beams," *IEEE Trans. Antennas Propag.*, vol. 62, no. 7, pp. 3543–3556, Jul. 2014.

[24] P. M. Rossini, L. Rossini, and F. Ferreri, "Brain-behavior relations: Transcranial magnetic stimulation: A review," *IEEE Eng. Med. Biol. Mag.*, vol. 29, no. 1, pp. 84–96, Feb. 2010.

[25] S. Debener, M. Ullsperger, M. Siegel, and A. K. Engel, "Single-trial EEG-fMRI reveals the dynamics of cognitive function," *Trends Cognit. Sci.*, vol. 10, no. 12, pp. 558–563, Oct. 2006.

[26] R. Jiang, B. H. Jansen, B. R. Sheth, and J. Chen, "Dynamic multi-channel TMS with reconfigurable coil," *IEEE Trans. Neural Syst. Rehabil. Eng.*, vol. 21, no. 3, pp. 370–375, Oct. 2013.

[27] J. Ruohonen and R. Ilmoniemi, "Focusing and targeting of magnetic brain stimulation using multiple coils," *Med. Biol. Eng. Comput.*, vol. 36, no. 3, pp. 297–301, May 1998.

[28] S. Yang, G. Xu, L. Wang, Y. Geng, H. Yu, and Q. Yang, "Circular coil array model for transcranial magnetic stimulation," *IEEE Trans. Appl. Supercond.*, vol. 20, no. 3, pp. 829–833, Mar. 2010.

[29] S. Ueno, T. Matsuda, and M. Fujiki, "Functional mapping of the human motor cortex obtained by focal and vectorial magnetic stimulation of the brain," *IEEE Trans. Magn.*, vol. 26, no. 5, pp. 1539–1544, Sep. 1990.

[30] S. Hui and W. W. Ho, "A new generation of universal contactless battery charging platform for portable consumer electronic equipment," *IEEE Trans. Power Electron.*, vol. 20, no. 3, pp. 620–627, May 2005.

[31] R. C. Hansen, *Electrically Small, Superdirective, and Superconducting Antennas*. New York, NY, USA: Wiley, 2006.

[32] C. A. Balanis, *Antenna Theory: Analysis and Design*. New York, NY, USA: Wiley, 2012.

[33] P. Overfelt, "Near fields of the constant current thin circular loop antenna of arbitrary radius," *IEEE Trans. Antennas Propag.*, vol. 44, no. 2, pp. 166–171, Feb. 1996.

[34] D. Werner and R. Mittra, "Lommel expansions in electromagnetics," in *Frontiers in Electromagnetics*. New York, NY, USA: Wiley, 2000, pp. 474–522.

[35] D. H. Werner, "An exact integration procedure for vector potentials of thin circular loop antennas," *IEEE Trans. Antennas Propag.*, vol. 44, no. 2, pp. 157–165, Feb. 1996.

[36] J. Fraleigh, R. Beauregard, and V. Katz, *Linear Algebra*, 3rd ed. Reading, MA, USA: Addison-Wesley, 1995.

Fei Gao (S'13) received the B.Sc. degree in electronic engineering and Ph.D. degree from Xidian University, Xi'an, China, in 2010 and 2015, respectively.

In 2010, he joined the National Laboratory of Science and Technology on Antennas and Microwaves (NLSTAM). In 2011, he joined the Antenna Measurement and Antenna Design Group, NLSTAM. From 2011 to 2012, he was responsible for global positioning system (GPS) antenna design with high phase center stability and ultra-wideband antenna design. Since 2012, he has been with the Applied Electromagnetics Research Group, University of California at San Diego, La Jolla, CA, USA, as a Visiting Graduate Student. His research interests include electrical small antennas (ESAs), ultra-wideband antennas, and near-field technology.

Fushun Zhang received the B.Sc., M.Sc., and Ph.D. degrees in electrical engineering from Xidian University, Xi'an, China, in 1982, 1993, and 1997, respectively.

In 2002 and 2008, he was involved with cooperative research as a Visiting Scholar with the City University of Hong Kong, the National Astronomical Observatory of Russia, the National Astronomical Observatory of Japan, and the Observatoire de Paris or Observatoire de Paris-Meudon. He is currently the academic leader in the field of electromagnetic wave and microwave technology with Xidian University. He has been involved in approximately 100 research projects, including the National Natural Science Foundation of China Genetic Algorithm (GA) in High Performance Antenna Design project. He has authored or coauthored over 200 technical publications. He holds a patent on small log-periodic antenna with high gain. His current research interests are antenna theory, design, and measurement.

Dr. Zhang is a member of the Chinese Institute of Electronics (CIE). He is a member of the Academic Committee, Key Laboratory of Structure Design of Electronic Equipment, Ministry of Education, China. He was the recipient of some awards for progress in science and technology of the Ministry of Electronics Industry, China.

Hiroki Wakatsuchi (M'11) was born in Toyama, Japan, in 1983. He received the B.Eng. and M.Eng. degrees in electrical and electronic engineering from Aoyama Gakuin University, Kanagawa, Japan, in 2006 and 2008, respectively, and the Ph.D. degree electrical and electronic engineering from the University of Nottingham, Nottingham, U.K., in 2011.

From 2005 to 2008, he was with the Electromagnetic Compatibility (EMC) Group, Applied Electromagnetic Research Center, National Institute of Information and Communications Technology (NICT), Japan . In 2008, he joined the George Green Institute for Electromagnetics Research (GGIEMR), Department of Electrical and Electronic Engineering, University of Nottingham. From 2011 to 2013, he was with the Applied Electromagnetics Group, Electrical and Computer Engineering Department, University of California at San Diego, La Jolla, CA, USA, as a Research Scholar. Since 2013, he has been with the Center for Innovative Young Researchers, Nagoya Institute of Technology, Nagoya, Japan, as an Assistant Professor. His current research interests include metamaterial research in both fundamentals and applications.

Dr. Wakatsuchi was the recipient of several awards including the York EMC Services Ltd. Best Paper Prize of the Festival of Radio Science URSI (2009), the Second Prize of the AP-RASC'10 Student Paper Competition, AP-RASC'10 (2010), the Asia–Pacific Radio Science Conference (2010), and the Funai Young Researcher Prize of the Funai Foundation for Information Technology (2014).

Daniel F. Sievenpiper (M'94–SM'04–F'09) received the B.S. and Ph.D. degrees in electrical engineering from the University of California at Los Angeles, Los Angeles, CA, USA, in 1994 and 1999, respectively.

He is currently a Professor with the University of California at San Diego, where his research is focused on antennas and electromagnetic structures. Prior to 2010, he was the Director of the Applied Electromagnetics Laboratory, HRL Laboratories in Malibu, CA, USA, where his research included artificial impedance surfaces, conformal antennas, tunable and wearable antennas, and beam-steering methods. He has authored or coauthored more than more than 80 technical publications. He holds 70 patents.

Dr. Sievenpiper has served as an associate editor for IEEE ANTENNAS AND WIRELESS PROPAGATION LETTERS since 2010. He currently serves as the chair of the IEEE Antennas and Propagation Society (AP-S) Committee on New Technology Directions. He was the recipient of the 2008 URSI Issac Koga Gold Medal.